Ordered Mesoporous Platinum@Graphitic Carbon Embedded Nanophase as a Highly Active, Stable, and Methanol-Tolerant Oxygen Reduction Electrocatalyst

Zhangxiong Wu,[†,‡] Yingying Lv,[‡] Yongyao Xia,[‡] Paul A. Webley,[†] and Dongyuan Zhao*[,†,‡]

[†]Department of Chemical Engineering, Faculty of Engineering, Monash University, Melbourne, VIC 3800, Australia
[‡]Department of Chemistry and Laboratory of Advanced Materials, Fudan University, Shanghai 200433, P. R. China

S *Supporting Information*

ABSTRACT: Highly ordered mesoporous platinum@graphitic carbon (Pt@GC) composites with well-graphitized carbon frameworks and uniformly dispersed Pt nanoparticles embedded within the carbon pore walls have been rationally designed and synthesized. In this facile method, ordered mesoporous silica impregnated with a variable amount of Pt precursor is adopted as the hard template, followed by carbon deposition through a chemical vapor deposition (CVD) process with methane as a carbon precursor. During the CVD process, in situ reduction of Pt precursor, deposition of carbon, and graphitization can be integrated into a single step. The mesostructure, porosity and Pt content in the final mesoporous Pt@GC composites can be conveniently adjusted over a wide range by controlling the initial loading amount of Pt precursor and the CVD temperature and duration. The integration of high surface area, regular mesopores, graphitic nature of the carbon walls as well as highly dispersed and spatially embedded Pt nanoparticles in the mesoporous Pt@GC composites make them excellent as highly active, extremely stable, and methanol-tolerant electrocatalysts toward the oxygen reduction reaction (ORR). A systematic study by comparing the ORR performance among several carbon supported Pt electrocatalysts suggests the overwhelmingly better performance of the mesoporous Pt@GC composites. The structural, textural, and framework properties of the mesoporous Pt@GC composites are extensively studied and strongly related to their excellent ORR performance. These materials are highly promising for fuel cell applications and the synthesis method is quite applicable for constructing mesoporous graphitized carbon materials with various embedded nanophases.
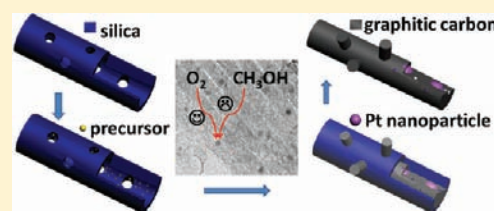
1. INTRODUCTION

Fuel cells such as direct methanol fuel cells (DMFCs) and proton exchange membrane fuel cells (PEMFCs) are highly desirable for automotive and portable electrical devices because they hold fascinating features including high energy density, low operating temperature, green emission, and ease of processing.[1,2] Their performance mainly relies on the electrochemical activities of the electrocatalysts toward fuel oxidation reaction (e.g., methanol oxidation reaction, MOR) at the anode and oxygen reduction reaction (ORR) at the cathode. Nanostructured and/or nanoporous platinum (Pt)-containing materials are the most common attractive electrocatalysts for both the anode and cathode in these fuel cells. Currently, the unsatisfactory activity, kinetics, and durability of the Pt-based ORR catalysts and the high Pt usage are the major bottlenecks for commercializing these fuel cells. As a result, extensive research has been devoted to developing new catalysts with enhanced ORR performance, including porous Pt nanostructures,[3−5] alloyed Pt nanoparticles,[6−8] carbon-supported Pt nanoparticles,[9−12] and some metal-free catalysts such as mesoporous nitrogen-enriched carbon materials.[13,14] Up to now, porous carbon-supported Pt nanoparticles are the most widely adopted ORR catalysts due to their reliable ORR performance as well as easy and scalable synthesis, such as the state-of-the-art and commercial carbon-black-supported Pt catalyst.[15]

Mesoporous carbon materials themselves or supporting functional composites are essential in many potential applications such as energy storage, catalysis, and adsorption and separation.[16−20] As supports for Pt nanoparticles in electrocatalysis, they can provide high surface area for finely dispersing nanoparticles, large pore size/volume for facilitating mass diffusion, and good electrical conductivity for providing sufficient electron pathways, thus leading to high Pt mass and/or specific activities.[9−12,21−31] However, major challenges still remain. First, the stability of the ORR electrocatalysts should be further improved. The most common support, carbon black, and some mesoporous carbon supports are mainly amorphous with high electrical resistance so that they are vulnerable to corrosion/oxidation, which can be further accelerated by the presence of Pt at high potentials (>0.7 V vs the normal hydrogen electrode, NHE), resulting in electrochemical isolation of Pt.[32] Meanwhile, the dispersed Pt nanoparticles have high surface energies and their interactions with amorphous carbon supports are fairly weak because in most

cases they are loosely dispersed in carbon matrices on which the surface oxides can further weaken the binding of Pt to carbon.[11] Consequently, detachment, aggregation and even dissolution of Pt nanoparticles occur during potential cycling and thus the fuel cell performance considerably degrades over time.[3] Using carbon supports with enhanced graphitic nature, such as carbon nanotubes, nanofibers, graphene, carbide-derived carbons and ordered mesoporous graphitic carbons, is an efficient way to strengthen the interactions between Pt and carbon and thus alleviate the above problem with enhanced utilization, activity and especially stability of Pt.[11,33−37] However, it is not easy to disperse Pt nanoparticles on graphitic carbon materials due to their relatively low surface areas and more importantly the lack of surface functionalities to adsorb an ionic Pt precursor. As a result, surface modification is normally required to get a good Pt dispersion,[38,39] which unfortunately could decrease the stability and electrical conductivity of the carbon supports as well as weaken the Pt−carbon interaction. Moreover, post loaded Pt nanoparticles tend to aggregate and/or ripen, leading to unsatisfactory stability. Second, previously reported ORR catalysts normally consist of a high Pt content (up to 50 wt %) and normally adopt a high Pt load on the electrode to obtain a high mass/specific activity and especially a good stability. Reduction of Pt usage while retaining the activity and durability is of significant importance for commercializing fuel cells. The third challenge is that the parasitic fuel oxidation (e.g., MOR) at the cathode caused by diffusion of fuel across the membrane is normally present and can result in degradation of ORR performance due to the poisoning of the catalyst and the occurrence of mixed potentials at the cathode.[6,40,41] Given the above challenges, new types efficient ORR electrocatalysts are still highly desirable.

Herein in this paper, we report the synthesis of a new type of ordered mesoporous graphitic carbon supporting Pt nanoparticles as a promising ORR electrocatalyst. The general idea is construction of an "embedded nanophase" that may be an efficient way to provide more active and stable catalysts (Scheme 1).[42] Specifically, Pt precursors $[Pt(NH_3)_4Cl_2 \cdot xH_2O]$ are first loaded into the ordered mesoporous SBA-15 template (Scheme 1a). The Pt species are highly dispersed in the mesopores without aggregation even at a very high loading content of ∼30 wt % (Supporting Information, Figure S1). Subsequently, chemical vapor deposition (CVD) with methane as a precursor is conducted at 900 °C,[18,43] leading to the simultaneous in situ decomposition/reduction of the preloaded Pt precursors to metallic Pt, deposition of graphitic carbon that embeds the Pt nanoparticles, formation of connected carbon networks (Scheme 1b), and growth of graphitized nanoflake structures on the outermost surface of the silica template. After removing the silica template, ordered mesoporous graphitic carbon materials with homogeneously dispersed Pt nanoparticles embedded in the graphitic carbon walls are obtained (denoted as Pt@GC, Scheme 1c,d). A detailed study shows that the ordered mesoporous Pt@GC composites with novel nanoarchitecture can serve as efficient ORR electrocatalysts, showing significantly improved Pt mass activities, large mesoporosities for fast reactant/product diffusion, highly graphitized carbon networks with high resistance to corrosion/oxidation, long-term stability under harsh fuel cell operating conditions, and good methanol tolerance to avoid the parasitic MOR at the cathode.

Scheme 1. Illustration of the Synthesis Procedure for the Ordered Mesoporous Pt@GC Composites^a
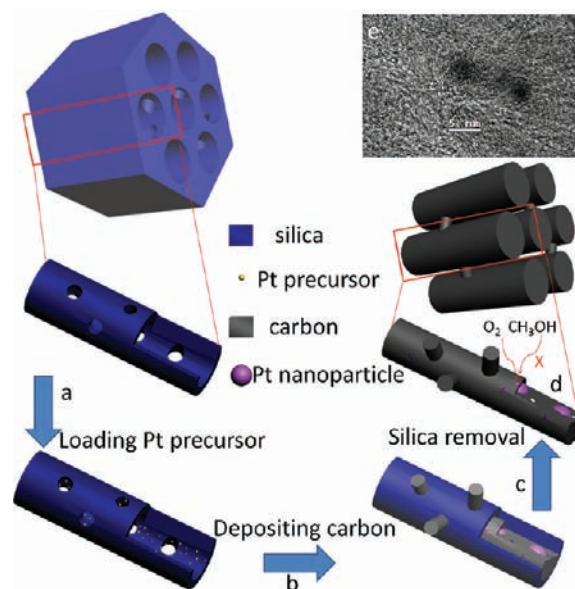
^{a}(a) Loading the Pt precursor into the mesopores of the silica template, (b) depositing graphitized carbon and formation of Pt nanoparticles during the CVD process at 900 °C for 3 h, (c) removing the silica template, (d) showing the Pt@GC embedded nanophase with micropores through which the Pt nanoparticles are accessible for O_2 diffusion but not easy for methanol infiltration, and (e) a representative TEM image showing the Pt@GC embedded nanophase.

2. EXPERIMENTAL SECTION

Chemicals. Triblock copolymer Pluronic P123 (M_w = 5800, $EO_{20}PO_{70}EO_{20}$), the Pt precursor $[Pt(NH_3)_4Cl_2 \cdot xH_2O]$, tetraethoxysilane (TEOS), isopropanol and Nafion solution (5 wt %) were purchased from Sigma-Aldrich. High-purity methane gas (99.99%) was obtained from Core Gas Company. Methanol and sulfuric acid were purchased from Shanghai Chemical Corporation. All the chemicals were used as received without further purification. Deionized water was used in all the experiments.

Synthesis of Ordered Mesoporous Pt@GC Composites. The ordered mesoporous SBA-15 was synthesized according to the reported procedure,[44] and was used as a hard template for the synthesis of mesoporous Pt@GC composites. The Pt precursor dissolved in water was first loaded into the mesochannels of the mesoporous SBA-15 template by a wet impregnation and then followed by solvent evaporation at ∼50 °C.[45] The loading amount of the Pt precursor could be varied over a wide range, typically 1−20 wt % for the synthesis of the mesoporous Pt@GC composites. Subsequently, ∼0.3 g of the dried SBA-15 loaded with a certain percentage of the Pt precursor was placed in a ceramic boat which was inserted into a tube furnace for CVD experiment. After a careful check to avoid gas leakage, the furnace was first heated to 600 °C (5 °C/min) under high-purity N_2 (99.999%, 100 mL/min). Then, the gas supply was switched from N_2 to methane (60 mL/min) at the point of 600 °C, followed by further increase of the temperature to 900 °C and held isothermal for 20 min ∼3 h to allow carbon deposition. After that, the furnace was naturally cooled down under N_2 atmosphere. The collected black products were immersed in a 10 wt % HF solution overnight to completely remove the silica template and recover the final mesoporous Pt@GC electrocatalysts. The preparation procedures for the counterpart catalysts for a comparative study were provided in the Supporting Information.

Measurements and Characterization. Wide-angle X-ray diffraction (XRD) patterns were recorded with a Bruker D4 X-ray

diffractometer (Germany) with Ni-filtered Cu Kα radiation (40 kV, 40 mA). Small-angle X-ray scattering (SAXS) patterns were recorded on a Nanostar U small-angle X-ray scattering system (Germany) also by using Cu Kα radiation (40 kV, 35 mA). Scanning electron microscopy (SEM) images were taken by a Hitachi S4800 or a JEOL 6300F scanning electron microscope (Japan) operated at an accelerated voltage of 1 or 20 kV. Samples were directly dispersed onto conductive tapes attached on a sample holder for direct observation under vacuum. Transmission electron microscopy (TEM) experiments were conducted on a JEOL 2100F (Japan) or a Phillips CM 20 (Netherland) microscope operated at 200 kV. The samples for TEM measurements were suspended in ethanol and dropped onto holey carbon film supported on Cu grids. Nitrogen adsorption/desorption isotherms were measured at −196 °C with a Micromeritics ASAP 2020 analyzer. Before the measurements, the samples were degassed in a vacuum at 180 °C for at least 8 h. The Brunauer−Emmett−Teller (BET) method and Barrett−Joyner−Halenda (BJH) model were adopted to analyze the surface areas (S_{BET}) and pore size distributions (D), respectively. The total pore volume (V_t) was calculated based on the N_2 adsorbed amount at a relative pressure of ∼0.995. Thermogravimetric (TG) analysis was conducted on a Mettler Toledo TGA/SDTA851 analyzer (Switzerland) from 25 to 900 °C (5 °C/min) under air (20 mL/min) to evaluate the Pt contents in the samples with each sample analyzed for at least two times for accuracy. X-ray photoelectron spectra (XPS) were measured by a Perkin-Elmer PHI5000C spectroscopy with Mg Kα line as the excitation source.

Electrochemical Test. Electrochemical tests such as cyclic voltammetry (CV) tests were measured on a CHI 606B electrochemical analyzer system (Shanghai CHI Instruments Co.) under ambient conditions. A three-electrode glass cell was used, in which a Pt wire was used as the counter electrode and a saturated calomel electrode (SCE, 0.2415 V vs the normal hydrogen electrode, NHE) as the reference electrode. The working electrode was made from the carbon-supported Pt catalysts and Nafion as a binder. Typically, ∼2.0 mg of a certain catalyst dispersed in 100 μL of isopropanol was mixed with 100 μL of a 0.5 wt % Nafion solution (in isopropanol) and ultrasonicated at room temperature for 30 min. Five μL of the above-prepared catalyst ink was injected onto a polished glassy carbon electrode and dried at ambient conditions for 15 min before electrochemical measurement. A 0.5 M H_2SO_4 solution in the presence or absence of 0.5 M CH_3OH was adopted as the electrolyte. CV measurements were conducted under N_2- or O_2-saturated conditions over a potential range of −0.2−1.2 V (vs SCE) with a scan rate of 2−50 mV/s, typically 10 mV/s. Potential cycling was conducted for ∼5 min before stable curves were recorded. The rotating disk electrode (RDE) technique was employed to study the ORR activity and kinetics with a rotating speed of 400−1600 rpm and a typical scan rate of 10 mV/s.

3. RESULTS AND DISCUSSION

3.1. Material Synthesis and Characterization. *3.1.1. Controllable Synthesis.* The mesostructure, porosity, as well as the Pt content in the final mesoporous Pt@GC composites can be individually or/and cooperatively controlled by tuning the CVD temperature and duration or/and controlling the initial loading amount of the Pt precursor (Scheme 1). Generally, a temperature of 900 °C is the optimized one for fast carbon deposition to synthesize ordered, high-surface-area and well-graphitized mesoporous carbon materials.[43] At this temperature, a considerable amount of graphitized carbon can be deposited within several minutes and the final mesoporous Pt@C composites possess variable high surface areas and large pore volumes (Figure S2A,B and Table S1). For example, a mesoporous Pt@GC sample with ∼12 wt % of Pt, ∼ 1330 m²/g of surface area and ∼2.0 cm³/g of pore volume was obtained by using a CVD time of 1 h and an initial Pt loading of ∼5 wt % (Figure S2A,b and Table S1). However, a CVD time

of 3 h is the most appropriate one to achieve a high carbon loading to faithfully replicate the ordered mesostructure and to avoid deposition of substantial extra carbon on the outer surface of the silica template (Figure S2C,c,f). Meanwhile, a higher initial Pt loading can lead to a better mesostructural regularity in the resultant mesoporous Pt@GC replica obtained with a shortened carbon deposition time (compare curve b and e in Figure S2C), due to the cofilling effect of Pt and carbon in the pore space of the template.[46] On the other hand, the Pt contents (1−30 wt %) in the final mesoporous Pt@GC composites can be also manipulated by tuning either the initial Pt loading amount (Figure S3A and Table S1) or the deposited carbon amount with different CVD time (Figure S3B and Table S1). As described above, the whole synthesis process can be finely controlled with the fulfillment of a series of novel mesoporus Pt@GC composites with variable properties. Hereafter, except for further clarification, we will only adopt the highly ordered mesoporous Pt@GC composites obtained with a CVD time of 3 h at 900 °C for demonstration.

3.1.2. Mesostructure and Porosity. SAXS patterns (Figure 1A) of the mesoporous Pt@GC composites with different Pt
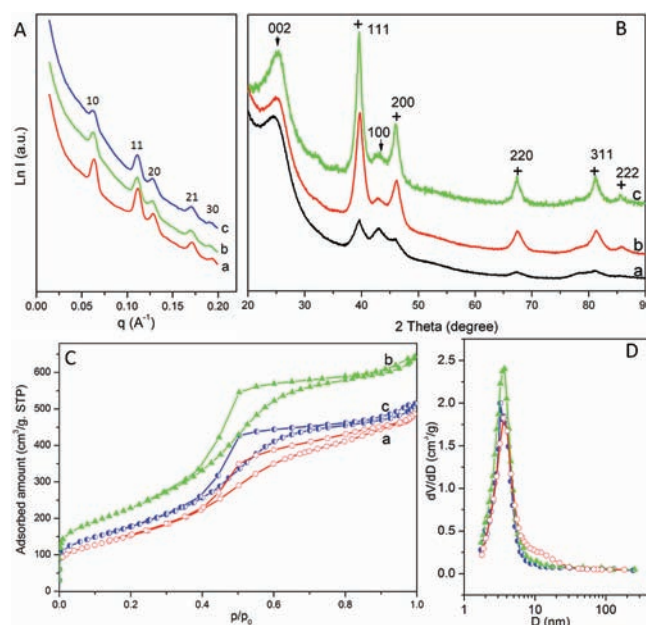
Figure 1. SAXS (A) and wide-angle XRD (B) patterns and N_2 sorption isotherms (C) and the corresponding pore size distribution curves (D) of the mesoporous Pt@GC composites with a Pt content of ∼2.0 (a), 3.5 (b), and 5.4 wt % (c), respectively.

contents (1−20 wt %, by controlling the initial Pt loading amount) obtained by using a CVD time of 3 h at 900 °C show five well-resolved diffraction peaks with very close cell parameters (Table S1), assigned to the 10, 11, 20, 21, and 30 reflections of a two-dimensional (2-D) hexagonal mesostructure, indicating a faithful replication. With the increase of Pt content, the intensities of the diffractions decrease to some extent, probably due to the fact that heavy metals can absorb X-rays and disturb the scatterings. Wide-angle XRD patterns (Figure 1B) show that the mesoporous Pt@GC composites possess graphitic carbon walls and well-crystallized Pt nanoparticles, showing high-intensity 002 and 100 diffractions (marked by arrows) belonging to graphitic carbon and the 111, 200, 220, 311, and 222 diffractions (marked by plus signs)

assigned to face-centered cubic metallic Pt (JCPDS card No. 04-0802). The sizes of the Pt nanoparticles are estimated to be 5−7.2 nm depending on the Pt content, namely, the higher the Pt content, the larger the particle size tends to be (Table S1). Notably, the sizes of the Pt nanoparticles are still limited to ~7.8 nm and finely dispersed in the carbon matrix even if the Pt content is up to ~20 wt % (Figure S4), indicating an excellent confinement that can avoid sintering of the Pt nanoparticles even at the very high temperature of 900 °C. Such superior confinement originates from the fact that the Pt species highly dispersed in the silica template are decomposed in situ and/or reduced to metallic Pt and simultaneously embedded by deposited carbon so that the resultant Pt nanoparticles are exclusively confined and isolated, leading to the high resistance toward sintering.

All the ordered mesoporous Pt@GC composites present typical type IV N_2 sorption isotherms with distinct H2 hysteresis loops (Figure 1C). The pore size distribution curves show very uniform mesopores centered at ~3.6 nm (Figure 1D and Table S1). Their pore wall thicknesses are approximately ~8.0 nm (Table S1), more or less larger than the sizes of the Pt nanoparticles. This indicates the nanoparticles can be fully embedded in the carbon walls. On the other hand, high surface areas (550−840 m^2/g) and large pore volumes (0.8−1.0 cm^3/g) are obtainable (Table S1). Interestingly, the mesoporous Pt@GC composites hold much higher surface areas and larger pore volumes than those of the ordered mesoporous Pt-free carbon material obtained at the same CVD conditions (Table S1), probably ascribed to the diffusion and transportation paths of small Pt clusters to form large nanoparticles during the thermal treatment, thus leading to microporosity in the carbon walls through which N_2 and O_2 molecules and electrolytes can diffuse onto the surface of the Pt nanoparticles. A notable amount of adsorbed N_2 over a low relative pressure range can be observed (Figure 1C). Correspondingly, the detailed pore size distribution calculated based on the density functional theory further reveals the existence of a uniform micropore size centered at ~1.2 nm (Figure S5), which is very important for facilitating the accessibility of the carbon-embedded Pt nanoparticles by gas molecules. For example, gravimetric sorption reveals that the Pt nanoparticles can approximately uptake stoichiometric H_2 at room temperature (Figure S6), suggesting that they are quite accessible for small gas molecules in spite of the carbon embedment.

3.1.3. Morphology and Fine Structure. Overall SEM images (Figure 2a,c,e) show that the mesoporous Pt@GC composites with different Pt contents have the same wheat-like morphology composed of bundles of nanorods as that of the mesoporous silica SBA-15 template.[44] No obvious aggregated Pt nanoparticles are observed, implying that they are well-confined in the carbon matrices without sintering. Interestingly, magnified SEM images (Figure 2b,d,f) present plenty of nanoflake structures attached on the outer carbon walls, resulting from extra graphitic carbon deposition/growth at the outer surface of the silica template. These structures are probably connected by the short carbon nanorods deposited in the complementary mesopores of the silica template. High-resolution SEM (HRSEM) images (inset in Figure 2a and Figure 2d) show the existence of ordered mesopore arrays in some broken areas. Elemental mapping (Figure 2g,h) presents evidence of a homogeneous dispersion of Pt. Another interesting phenomenon observed is that a small fraction of carbon nanotubes are also visible (Figure 2f) for the sample
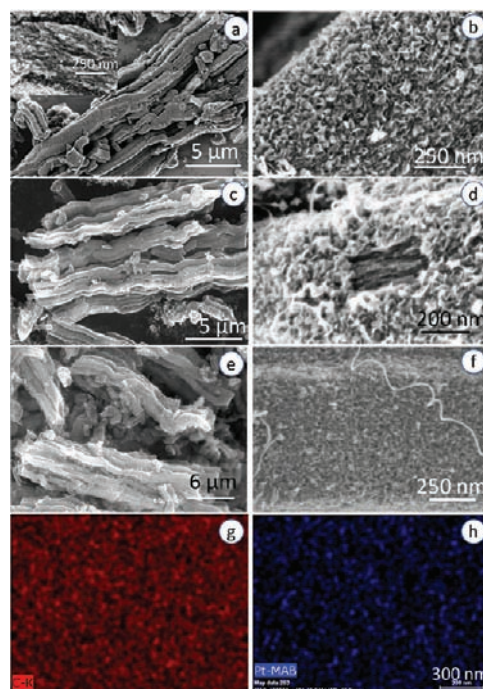
Figure 2. SEM (a−f) and HRSEM (inset in a) images and the C (g) and Pt (h) elemental mapping results of the mesoporous Pt@GC composites with a Pt content of ~2.0 (a and b), 3.5 (c and d), and 5.4 wt % (e−h), respectively.

with a high Pt content of ~5.4 wt %, probably arising from the catalytic growth of carbon nanotubes over a small fraction of Pt that is not confined during the loading and carbon deposition processes. These carbon nanotubes are probably formed during the cooling step after the CVD process at 900 °C because it is difficult to grow carbon nanotubes from methane at this temperature. Nevertheless, even with a high initial Pt loading (e.g., ~10 wt %), the amount of carbon nanotubes grown can be well controlled by adjusting the CVD time. A deposited time of 20 min gives rise to a low amount of deposited carbon (~0.46 g/g SiO_2). In this case, some Pt nanoparticles are not or at least not fully embedded with carbon, and they can probably diffuse toward the outer surface. As a result, these exposed Pt nanoparticles can catalyze the growth of bundles of carbon nanotubes (Figure S7a-c). At a longer CVD time of 1 h, a much higher amount (~0.67 g/g SiO_2) of deposited carbon is achieved so that the Pt nanoparticles are more severely embedded, and thus much fewer carbon nanotubes can be catalytically grown (Figure S7d-f). Finally, at a time of 3 h, the deposited carbon amount (~1.2 g/g SiO_2) can almost fully fill up the pore voids of the silica template. Thus, the Pt nanoparticles are almost completely embedded, and only several carbon nanotubes can be occasionally observed (Figure S7g,h). Moreover, in the samples with considerable amounts of carbon nanotubes, the Pt nanoparticles with high contents (up to 15 wt %) are still homogeneously dispersed with the particle sizes at ~8 nm (Figure S7c,f). Meanwhile, the carbon nanotubes attached on the outer walls may be helpful for enhancing electrical conductivity.

Representative TEM images (Figure 3a,d,g) of the mesoporous Pt@GC composites with different Pt contents show ordered mesopore arrays in large domains. Notably, finely and uniformly dispersed Pt nanoparticles are observed and the particle density gradually increases with the enhancement of Pt
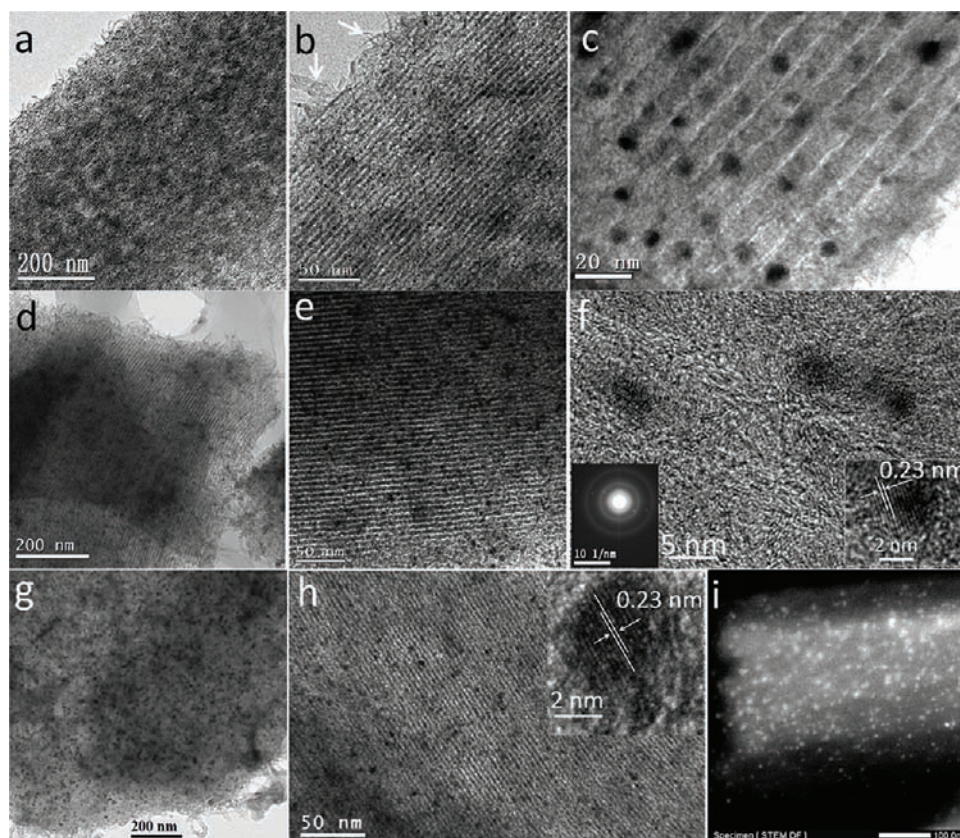
Figure 3. TEM (a−c, d−e, and g−h), HRTEM (f, right inset in f and inset in h) images, SAED pattern (left inset in f) and DF-STEM image (i) of the mesoporous Pt@GC composites with a Pt content of ∼2.0 (a−c), 3.5 (d−f), and 5.4 wt % (g−i), respectively.

content. Magnified TEM observations further present uniformly dispersed dark-contrasted dots with increasing density (Figure 3b,e,h). Remarkably, most of the nanoparticles are located within the carbon walls. High-magnification TEM and HRTEM images (Figure 3c,f) further reveal that the Pt nanoparticles are mostly embedded by the carbon walls (especially in the case of a low Pt content) instead of dispersed in the mesopores or aggregated out of the pore walls. The embedded Pt nanoparticles are estimated to be 4.0−7.5 nm, in good agreement with the wide-angle XRD results. The pore wall thickness is estimated to be ∼8.0 nm, in accordance with the N$_2$ sorption and SAXS results. Moreover, the carbon walls are well graphitized (Figures 3f and S8a) especially for the edge carbon walls, showing layer-like lattices with a d-spacing of ∼0.34 nm. It is further illustrated by the selected area electron diffraction (SAED) pattern presenting bright diffraction rings assigned to graphitic carbon (left inset in Figure 3f). The nanoflake structures can also be directly observed (marked by arrows in Figure 3b), which are highly graphitized (Figure S8b). The graphitic nature of the carbon matrix is also supported by elemental analysis showing a low content of oxygen (Figure S9). HRTEM images (insets in Figure 3f,h) reveal that the Pt nanoparticles are highly crystalline showing diffraction spots in the SAED pattern (left inset in Figure 3f) and well-resolved lattices of ∼0.23 nm identified as the d-spacing of the (111) plane of face-centered cubic Pt. Furthermore, a typical dark-field scanning TEM (DF-STEM) image (Figure 3i) of the mesoporous Pt@GC composite with a Pt content of ∼5.4 wt % shows a uniform dispersion of bright dots, indicating the Pt nanoparticles are highly confined and uniformly dispersed. Even with a much higher Pt content (∼20 wt %), the

nanoparticles are still finely dispersed and embedded or/and anchored within the carbon walls (Figure S4c,d). Due to the confinement and embedment effects, the surface-sensitive XPS spectra (Figures S10A,a and S10B,a) reveal that almost no Pt is detected for the mesoporous Pt@GC composite with ∼5.4 wt % of Pt, further suggesting that the Pt nanoparticles are exclusively confined.[47]

3.2. Electrochemical Properties. *3.2.1. ORR Activity.* The ordered mesoporous Pt@GC composites can be adopted as efficient electrocatalysts for ORR, showing high mass and specific activities, a long cyclic stability and a methanol-tolerant behavior (see details below). The CV curve (Figure 4A, a) recorded by using the mesoporous Pt@GC composite with ∼5.4 wt % of Pt as the electrode under N$_2$-saturated H$_2$SO$_4$ (0.5 M) presents two redox peaks at ∼0.35 V (all the voltages in this paper are versus SCE), similar to the mesoporous Pt-free carbon matrix (Figure S11), due to the formation/reduction of Pt oxide and/or surface oxides on the carbon matrix. There is a high capacitance due to the large surface area,[12,35] thus masking the detailed hydrogen adsorption/desorption features in the CV curve. However, small shoulder peaks at ∼−0.185 V associated with hydrogen desorption/adsorption are observed, which are absent for the mesoporous Pt-free carbon (Figure S11), indicating there exist many Pt active sites in the mesoporous Pt@GC composite. When the CV curve is recorded under O$_2$-saturated H$_2$SO$_4$ electrolyte, the curve part at a voltage of >0.55 V almost overlaps with that obtained under N$_2$-saturated electrolyte, but the current density at a voltage of <0.55 V is significantly enhanced (Figure 4A,b). However, the current intensity over the whole potential range for the mesoporous Pt-free carbon support is changeless

2240

dx.doi.org/10.1021/ja209753w | *J. Am. Chem. Soc.* 2012, 134, 2236−2245
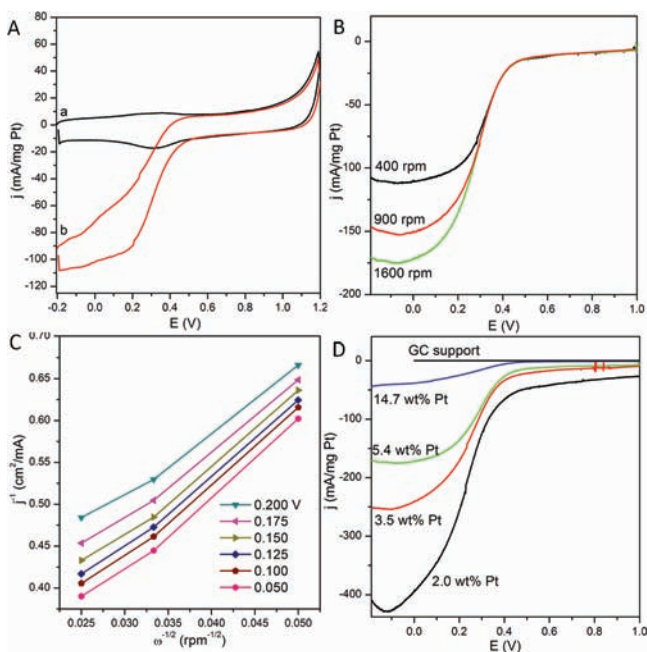
Figure 4. CV curves (A) recorded under N_2- (a) and O_2-saturated (b) 0.5 M H_2SO_4 electrolyte, polarization profiles (B) recorded under O_2-sparging electrolyte at 400−1600 rpm, and the corresponding Koutecky−Levich plots (C) at various potentials of the mesoporous Pt@GC composite with a Pt content of ∼5.4 wt %; (D) is the polarization profiles of the mesoporous Pt@GC composites with different contents of Pt recorded at 1600 rpm. The scan rates are all set at 10 mV/s.

(Figure S11), suggesting that the mesoporous Pt@GC composite possesses a high ORR activity. The polarization profiles (Figure 4B) of the mesoporous Pt@GC composite with 5.4 wt % of Pt recorded in O_2-sparging electrolyte show well-defined diffusion limiting currents (−0.2 to +0.2 V) followed by a mixed kinetic-diffusion control region over a potential window of 0.2−0.6 V. The current density is obviously enhanced with the rotating speed increasing from 400 to 1600 rpm, achieving a superior apparent mass activity of ∼27 and 10 mA/mg Pt at 0.4 and 0.6 V and a limiting mass activity of ∼175 mA/mg Pt at 1600 rpm, much higher than those of many carbon-supported Pt catalysts previously reported. Moreover, the ORR activity is quite stable at different scan rates from 2 to 50 mV/s (Figure S12). The corresponding Koutecky−Levich plots (j^{-1} vs $\omega^{-1/2}$) at several potentials (Figure 4C) exhibit good linearity with the slopes remaining generally constant, suggesting that the electron transfer numbers of ORR at the different potentials are similar. The electron transfer number is calculated to be ∼3.70 according to the Koutecky−Levich equation (see the Supporting Information for details), indicating a four-electron transfer mechanism. The limiting kinetic current at 0.1 V is calculated to be ∼6.5 mA/cm^2, giving a further evidence of high ORR activity. The superior mass activity is further demonstrated by the polarization curves of the ordered mesoporous Pt@GC composites with different Pt contents of 2.0−14.7 wt % (Figure 4D), achieving a limiting apparent mass activity of ∼400 mA/mg Pt for the mesoporous Pt@GC composite with ∼2.0 wt % of Pt and a value of 40 mA/mg Pt is obtained even if the Pt content is enhanced to ∼14.7 wt %, better than those of many reported catalysts.[33,35] The inferior mass activity of the sample with a higher content of Pt is mainly due to the relatively larger

particle sizes. In developing Pt-based ORR electrocatalysts, it is a general target to reduce the Pt usage down to 0.1 mg/cm^2 or lower.[40] Herein in our results, the Pt load is as low as ∼5.6 μg/cm^2 but shows a superior mass activity. Such promising performance is attributed to the integration of several desired features in the ordered mesoporous Pt@GC composites and will discussed in detail later (see section 3.3).

3.2.2. Comparison of ORR Activity. To further demonstrate the superior ORR mass activity of the mesoporous Pt@GC composites, a series of counterpart catalysts were also prepared (see details in the Supporting Information) and tested for ORR as comparison, including two commercial catalysts with ∼5.6 and 36 wt % of Pt highly dispersed in a mainly microporous activated carbon support (Figure S13), an ordered mesoporous Pt-GC catalyst with the Pt nanopartices (3.7 wt % of Pt) not embedded in the carbon walls but highly dispersed in a similar graphitic carbon support (Figure S14), and two catalysts with ∼2.4 and 12 wt % of Pt highly dispersed in an ordered mesoporous amorphous CMK-3 carbon support (Figure S15). Experiments were conducted under the same conditions for comparison, namely, an O_2-sparging 0.5 M H_2SO_4 electrolyte, a scan rate of 10 mV/s, a rotating speed of 1600 rpm and a similar Pt load on the electrode. Having a similar Pt content (∼5.4 wt %), the mesoporous Pt@GC composite (Figure 5A,a) shows an overwhelmingly higher mass activity than that of the commercial catalyst (Figure 5A,b) consisting of smaller Pt nanoparticles (∼3.5 nm, Figure S13a-d), suggesting that the ordered graphitic carbon support with regular mesopores is advantageous over the mainly microporous (with some disordered mesopores) carbon support to promote the accessibility of Pt, infiltration and diffusion of electrolyte, and mass transfer during the electrochemical reactions. Having a similar Pt content (∼3.5 wt %), the mesoporous Pt@GC composite (Figure 5A,c) also shows a much better mass activity than that of the mesoporous Pt-GC catalyst (Figure 5A,d), indicating the accessible Pt active sites are much fewer in the latter due to the relatively lower degree of Pt dispersion, larger particle sizes and the inferior interfacial interaction between the carbon support and Pt (Figure S14). Furthermore, with a similar Pt content (∼2.0 wt %), the mesoporous Pt@GC composite (Figure 5A,e) also shows a better mass activity compared with that (Figure 5A,f) of the mesoporous carbon CMK-3-supported Pt catalyst consisting of Pt nanoparticles of 3−8 nm (Figure S15a-e), indicating that a graphitic nature of the carbon support is much favored for faster electron transportation with a lower electrical resistance. Moreover, the most important aspect is that the cyclic stability of the amorphous-carbon-supported catalyst is far inferior to those of the graphitic-carbon-supported catalysts (see section 3.2.3). Finally, the ORR mass activity of the mesoporous Pt@GC composite is also predominantly better than that of the commercial catalyst with a much higher Pt content of ∼36 wt % (Figure 5A,g), suggesting that a substantial reduction of Pt usage can be achieved while retaining a high mass activity for the mesoporous Pt@GC catalysts. On the other hand, in order to get a better specific activity, a higher Pt load on the electrode is generally required. The mesoporous Pt@GC composite with a Pt load of ∼15 μg/cm^2 (Figure 5B,a) shows a similar limiting specific activity (∼2.6 mA/cm^2) as that of the pure Pt electrode (Figure 5B,b), but the half-wave potential is obviously higher for the former, indicating a better kinetic activity. Moreover, with a similar Pt load of ∼60 μg/cm^2 on the electrode, the mesoporous Pt@GC composite presents a much better limiting
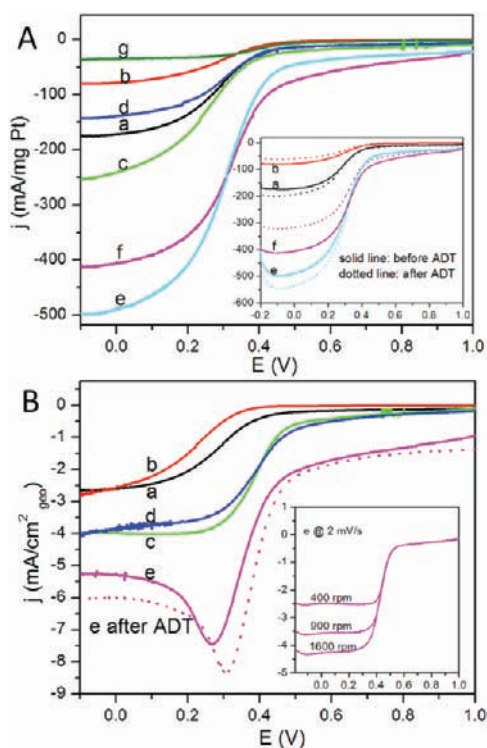
Figure 5. Polarization profiles in the mass activity (A) of the mesoporous Pt@GC composite with ~5.4 wt % of Pt (a); commercial activated carbon supported catalyst with ~5.6 (b) and 36 wt % (g) of Pt; Pt@GC composite with ~3.5 wt % of Pt (c); Pt-GC catalyst with ~3.7 wt % of Pt (d); Pt@GC composite with ~2.0 wt % of Pt (e) and CMK-3 supported catalyst with ~2.4 wt % of Pt (f) recorded under O_2-sparging 0.5 M H_2SO_4 electrolyte at 1600 rpm. Inset (A) is the corresponding comparative curves before and after ADT. (B) is the polarization profiles in the specific activity of the mesoporous Pt@GC composite with ~5.4 wt % of Pt (a, e); pure Pt electrode (b); mesoporous CMK-3 supported catalyst with ~12 wt % of Pt (c) and commercial activated carbon supported catalyst with ~36 wt % of Pt (d). The Pt load on the elctrode is ~15 (A, a−b and B, a), 10 (A, c−d), 6 (A, e−f), 60 (B, c,e), and 110 $\mu g/cm^2$ (B, d), respectively. The dotted line in (B) is the corresponding curve after ADT. All the scan rates are set at 10 mV/s except that the polarization profiles (inset in B) of the mesoporous Pt@GC composite with ~5.4 wt % Pt and a Pt load of ~60 $\mu g/cm^2$ were also recorded at a scan rate of 2 mV/s.

specific activity (~6.0 mA/cm², Figure 5B,e) than that (~4.0 mA/cm², Figure 5B,c) of the CMK-3-supported Pt catalyst with ~12 wt % of Pt (Figure S15f-j). It is also better than that (~4.0 mA/cm², Figure 5B,d) of the commercial catalyst containing 36 wt % of Pt (Figure S13e-h) even using a higher Pt load of ~110 $\mu g/cm^2$. It is interesting to note that there is a current peak in the polarization curve of the mesoporous Pt@GC composite with a high Pt load of ~60 $\mu g/cm^2$ when using a scan rate of 10 mV/s (Figure 5B,e), which can be avoided with a lower scan rate of 2 mV/s (inset in Figure 5B). This phenomenon is probably because part of the thick catalyst layer is not utilized for reducing oxygen under a fast scan rate due to the insufficient time to allow electrolyte and O_2 molecules to diffuse deep into the whole thick catalyst layer. The above results clearly demonstrate that both high mass and specific activities can be achieved with much less Pt usage on the electrode by using the mesoporous Pt@GC composites as the catalysts, which is highly desirable for lowering the cost of fuel cells. It should be noted that the relatively lower half-wave

potentials of the Pt@GC and counterpart catalysts compared with some values reported previously are mainly due to the different measurement conditions.

3.2.3. Durability. Durability of the ORR catalysts is a major concern. Herein, in order to evaluate the durability of the mesoporous Pt@GC catalysts, a standard accelerated durability test (ADT) by potential cycling (2000 cycles) at 0−0.8 V with a scan rate of 50 mV/s under N_2-saturated 0.5 M H_2SO_4 electrolyte was conducted. The ORR mass activities for the mesoporous Pt@GC catalysts after ADT are enhanced to some extent (the inset curves a and e in Figure 5A), indicating a high durability of the catalysts. The relatively lower initial mass activity before ADT is probably due to the hydrophobic nature of the carbon support so that it is required some time to allow O_2 molecules and the aqueous electrolyte to diffuse into and wet the whole carbon mesopores. On the contrary, after the same ADT test, the mass activities of all the counterpart catalysts decrease obviously by about ~20%. For example, the ORR mass activity of the CMK-3-supported Pt catalyst drops down by ~25% after the ADT (inset curve in Figure 5A). To further verify the excellent stability, potential cycling under more harsh condition of −0.2−1.2 V with a scan rate of 50 mV/s was conducted because the voltage under fuel cell operations can be up to ~1.5 (vs NHE) at worst conditions.[36,48] After cycling for 10 h, there is no obvious carbon oxidation of the GC support and the ORR activity is even slightly enhanced (dotted line in Figure 5B,e), while severe carbon oxidation of the CMK-3 support and significant loss of ORR activity are observed (data not shown). TEM images of the mesoporous Pt@GC composite after the above harsh cyclic test still present uniformly dispersed Pt nanoparticles that are still mostly embedded in the carbon walls without obvious aggregation and/or Oswald ripening (Figure 6a−c). HRTEM images show that the Pt nanoparticles are crystalline and the carbon walls are still graphitic without destruction of the ordered mesostructure (Figure 6d,e). However, for the CMK-3 supported Pt catalyst, after the above cyclic test, severe aggregation and Oswald ripening of the Pt nanoparticles is observed (Figure 6f−h). Moreover, the ordered mesostructure is greatly damaged due to the oxidation of the amorphous carbon support (Figure 6f,g). The above results clearly demonstrate the excellent stability of the mesoporous Pt@GC catalysts.

3.2.4. Methanol Tolerance. Another important characteristic of the mesoporous Pt@GC catalysts is that they are methanol tolerant during ORR operation, which is favored for developing DMFCs because the methanol-tolerant property means that more methanol can be fed at the anode and the poisoning effect could be mitigated at the cathode.[12] The CV curve (solid line in Figure 7A,a) of the mesoporous Pt@GC catalyst (~ 5.4 wt % of Pt) recorded under N_2-saturated H_2SO_4 electrolyte in the presence of methanol (0.5 M) almost overlaps with that recorded in the absence of methanol (dotted line in Figure 7A,a). Meanwhile, the corresponding CV curve (solid line in Figure 7A,b) recorded under O_2-saturated H_2SO_4 electrolyte in the presence of methanol also almost overlaps with that recorded in the absence of methanol (dotted line Figure 7A,b). These results clearly indicate that the mesoporous Pt@GC catalyst holds good electrocatalytic selectivity toward ORR without noticeable activity for MOR. The polarization profiles also present similar ORR activity in the presence and absence of methanol (inset in Figure 7A). On the contrary, the counterpart catalysts with the similar Pt
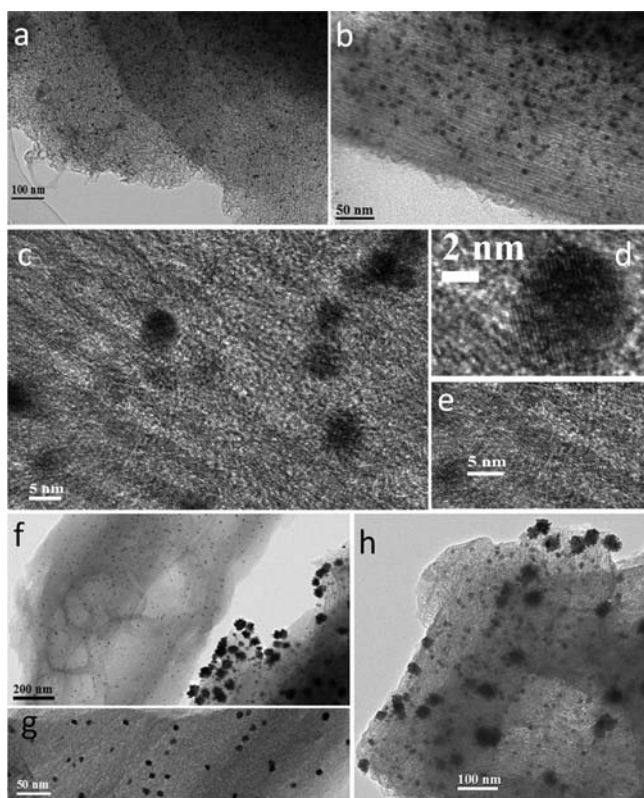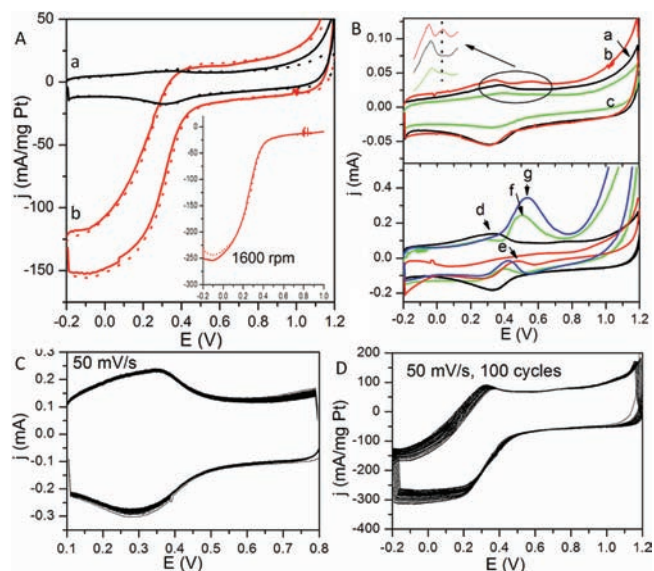
Figure 6. TEM (a–c, f–h) and HRTEM (d, e) images of the mesoporous Pt@GC composites with a Pt content of ∼5.4 wt % (a–e) and the mesoporous CMK-3 supported catalyst with a Pt content of ∼2.4 wt % (f–h) after the ADT measurement over a potenl range of −0.2 to +1.2 V.

Figure 7. CV curves (A) of the mesoporous Pt@GC composite with a Pt content of ∼5.4 wt % recorded in N_2- (a) and O_2-saturated (b) 0.5 M H_2SO_4 electrolyte in the absence (solid lines) and presence (dotted lines) of 0.5 M methanol. Inset (A) is the corresponding polarization profiles recorded under O_2-sparging electrolytes. CV curves (B) of the mesoporous Pt@GC composite with ∼5.4 wt % of Pt (a, d); Pt-GC catalyst with ∼3.7 wt % of Pt (b); commercial activated carbon supported catalysts with ∼5.6 (c) and 36 wt % (f) of Pt; pure Pt electrode (e) and mesoporous CMK-3 supported catalyst with ∼12 wt % of Pt (g) recorded under O_2-sparging 0.5 M H_2SO_4 in the presence of 0.5 M methanol. The Pt load on the electrode shown in (B) is ∼15 (a, c), 10 (b), 60 (d, g) and 110 $\mu g/cm^2$ (f), respectively. (C) and (D) are the potential cycling for 100 times recorded in N_2- and O_2-sparging 0.5 M H_2SO_4 electrolyte in the presence of 0.5 M methanol, respectively.

content and Pt load show obvious MOR signals under N_2-staturated H_2SO_4 electrolyte in the presence of methanol (Figure 7B, curves b and c, and the inset magnified curves showing the current signals for MOR). More evidently, there is still no obvious MOR signal for the mesoporous Pt@GC catalyst with a high Pt load of ∼60 $\mu g/cm^2$ (Figure 7B,d). However, the pure Pt electrode (Figure 7B,e), the commercial catalyst with a Pt load of ∼110 $\mu g/cm^2$ (Figure 7B,f) and the CMK-3-supported Pt catalyst with the same Pt load of ∼60 $\mu g/cm^2$ (Figure 7B,g) show high MOR activities, which are harmful for ORR at the cathode. Furthermore, even after 100 cycles of CV measurements under N_2-saturated H_2SO_4 electrolyte in the presence of methanol, there is still no obvious MOR signal observed for the mesoporous Pt@GC catalyst (Figure 7C). Meanwhile, the ORR activity is well retained after 100 CV cycles under O_2-sparging H_2SO_4 electrolyte in the presence of methanol (Figure 7D), clearly suggesting a methanol-tolerant and stable ORR activity of the mesoporous Pt@GC catalysts.

3.3. Insight into Structure-Performance Connection. The ordered mesoporous Pt@GC composites show promising performance as ORR electrocatalysts which is found to be well correlated with their novel nanoarchitecture and framework properties. First, the significantly improved Pt mass activity is ascribed to four factors: (1) the higher surface areas of the mesoporous graphitized carbon support compared with conventional ones can promote homogeneous dispersion of Pt nanoparticles even with a high content up to ∼20 wt % (Figure S4) so that there are abundant Pt active sites; (2) the graphitized mesopore walls with attached graphitic nanoflake

structures (Figure 3 and Figure S8) can provide sufficient and fast electrical pathways so that the Pt sites are electrochemically active; (3) the mesoporous Pt@GC "embedded nanophase" can provide a large and intimate interface between carbon and Pt so that the Pt nanoparticles possess high active surface areas;[49] (4) the microporous nature (Figure S5) of the carbon walls and the regular mesoporous structure can facilitate mass diffusion and transportation so that the active Pt sites are accessible for small gas molecules (Figure S6). As a result of the combination of the above features, the mesoporous Pt@GC composites provides excellent ORR mass activity, better than those of the counterpart Pt catalysts supported on mainly microporous activated carbon, mesoporous amorphous carbon, and mesoporous graphitic carbon with an inferior Pt to carbon binding. Experimental results show that the Pt nanoparticles in the mesoporous Pt@GC catalyst with ∼5.4 wt % of Pt are still electrochemically active even by coating a very thick layer of catalyst ink on the working electrode (data not shown).

The superior stability of the mesoporous Pt@GC catalysts is mainly due to two factors. On one hand, the highly graphitized carbon support is far more resistant to oxidation compared to amorphous carbons. TG curves show that the oxidation of the graphitic carbon support in air in the mesoporous Pt@GC composites starts at ∼520 °C (Figure S3A,a−d) while the activated carbon and the mesoporous CMK-3 supports in the counterpart catalysts start to be oxidized at a lower temperature of ∼420 °C (Figure S3A,e). As a result, the mesoporous graphitic carbon support is more stable against degradation

during potential cycling (Figure 6).[50] On the other hand, the Pt nanoparticles in the mesoporous Pt@GC composites are also more stable during potential cycling attributed to the intimate interface between Pt and carbon as well as the embedment of Pt by carbon. It is reported that surface oxides bound to carbon in amorphous carbon can withdraw electrons, thus dramatically weakening the interaction between Pt and carbon.[11] As a result, potential cycling leads to continuous oxidation of the carbon support causing destruction of the CMK-3 support (Figure 6f–h) and detachment/aggregation or even dissolution of the supported Pt nanoparticles (Figure 6f–h), leading to considerable deterioration of ORR performance. On the contrary, for the mesoporous Pt@GC composites, the content of surface oxide is relatively low (∼4 wt % of O by XPS) and there are strong binding interactions between Pt and carbon due to the electron delocalization between the π sites of carbon and the d orbital of Pt (covalent), as well as electron transfer from Pt to carbon (ionic).[11,48,50] XPS spectra show that the predominant component of C1s peaks of the mesoporous Pt@GC composites show high binding energies (∼285.7 eV, Figure S10C,a,b) compared with those of the commercial activated carbon and the mesoporous carbon CMK-3 supports (∼284.6 eV, Figure S10C,c,d), suggesting an enhanced carbon to Pt binding. More evidently, the Pt $4f_{7/2}$ peaks of the mesoporous Pt@GC composites shift to high binding energies (∼72.7 eV, Figure S10B,a,b) compared with those of unsupported Pt (∼71.0 eV), the commercial activated carbon supported catalyst (∼71.9 eV, Figure S10B,d), and the CMK-3 supported catalyst (∼71.8 eV, Figure S10B,c), clearly indicating an enhanced binding of Pt to carbon. Moreover, unlike previous reports, in the mesoporous Pt@GC composites, the Pt nanoparticles are embedded in graphitic carbon walls with a large interface and an excellent confinement effect, thus further mitigating Pt dissolution, Ostwald ripening, and coalescence during harsh potential cycling. The synergic effects that combine graphitized carbon, homogeneously dispersed and embedded Pt nanoparticles, and strong Pt to carbon binding finally lead to the excellent durability of the mesoporous Pt@GC catalysts.[10,25,46,51]

The methanol-tolerant behavior of the mesoporous Pt@GC catalysts is mainly due to two factors. On the one hand, the novel carbon embedment property with microporous carbon walls renders the embedded Pt nanoparticles easily accessible by gas molecules like H_2 and O_2 to maintain a high ORR activity and fast kinetics,[12,46b,51] while dramatically hindering methanol diffusion and infiltration. On the other hand, a careful HRTEM study (insets in Figure 3f,h) reveals that most Pt nanoparticles show Pt (111) planes, which are favored for ORR but much less active for MOR,[51−53] thus may also account for the methanol-tolerant behavior.

4. CONCLUSIONS

Highly ordered mesoporous and well-graphitized carbon materials with high surface areas and finely dispersed Pt nanoparticles have been designed and synthesized through a CVD-assisted nanocasting method by using ordered mesoporous silica SBA-15 as a hard template. In this novel method, a Pt precursor of variable concentration is first loaded into the silica template. During the subsequent CVD process, in situ decomposition/reduction of the preloaded Pt precursor, deposition of carbon and graphitization are integrated into a single step. The mesostructure with either disordered or ordered mesopores, porosity with surface areas of 550−1400

m^2/g and pore volumes of 0.75−2.0 cm^3/g, Pt contents of 0−30 wt % and growth of carbon nanoflakes or nanotubes in the final mesoporous Pt@GC composites can be well controlled over the wide ranges by individually and/or cooperatively manipulating the initial loading amount (1−50 wt %) of the Pt precursor and the CVD time of 20 min ∼3 h at 900 °C. In these obtained mesoporous Pt@GC composites, the Pt nanoparticles are homogeneously dispersed and highly embedded within the graphitic carbon pore walls, unlike previous reports with the Pt nanoparticles post loaded and loosely dispersed in/out of the mesopores of the carbon matrices. Meanwhile, the microporous nature of the carbon networks makes the uniformly dispersed and embedded Pt nanoparticles readily accessible by gas molecules but reduces methanol infiltration. The integration of high surface area, regular mesopores, graphitic nature of the carbon support as well as the highly dispersed and spatially imbedded Pt nanoparticles in the mesoporous Pt@GC composites make them excellent as ORR electrocatalysts which we have shown through systematic study. The high mesoporosity with the microporous nature, well-graphitized carbon support and large interface between carbon and Pt lead to a significant Pt mass activity toward ORR. Meanwhile, the high resistance of the graphitic carbon support toward oxidation, strong Pt to carbon binding with a large and intimate interface and the excellent confinement effect provide an excellent long-term stability over harsh potential cycling. In addition, the carbon embedment effect makes it difficult for methanol to infiltrate to the Pt active sites resulting in a methanol-tolerant behavior. The combination of the above features makes the mesoporous Pt@GC composites highly promising for fuel cell applications. Finally, the synthesis method is also quite applicable for rational design of other embedded nanophases in ordered mesoporous graphitic carbon materials.

■ ASSOCIATED CONTENT

ⓢ Supporting Information
Experimental details regarding the preparation of the several counterpart porous carbon supported Pt catalysts; details for calculating the Koutecky−Levich plots; TEM images of the mesoporous SBA-15 template loaded with Pt precursor; comprehensive supporting data of SAXS and wide-angle XRD patterns, N_2 sorption results, H_2 adsorption results, TG analyses, SEM and TEM images, and XPS spectra of the mesoporous Pt@GC composites prepared under various conditions; supporting data of CV curves and polarization profiles of the mesoporous Pt-free carbon and the mesoporous Pt@GC composites; extensive characterization results of the several counterpart porous carbon supported Pt catalysts; detailed summary of the structural, textural and compositional properties of all the studied catalysts; complete ref 41. This material is available free of charge via the Internet at http://pubs.acs.org.

■ AUTHOR INFORMATION

Corresponding Author
dyzhao@fudan.edu.cn

■ ACKNOWLEDGMENTS

2244

dx.doi.org/10.1021/ja209753w | J. Am. Chem. Soc. 2012, 134, 2236−2245

■ REFERENCES

(1) Ji, X. L.; Lee, K. T.; Holden, R.; Zhang, L.; Zhang, J. J.; Botton, G. A.; Couillard, M.; Nazar, L. F. *Nat. Chem.* **2010**, *2*, 286.

(2) Winter, M.; Brodd, R. J. *Chem. Rev.* **2004**, *104*, 4245.

(3) Sun, S. H.; Zhang, G. X.; Geng, D. S.; Chen, Y. G.; Li, R. Y.; Cai, M.; Sun, X. L. *Angew. Chem. Int. Chem* **2011**, *50*, 422.

(4) Liang, H. W.; Cao, X. A.; Zhou, F.; Cui, C. H.; Zhang, W. J.; Yu, S. H. *Adv. Mater.* **2011**, *23*, 1467.

(5) Yeo, K. M.; Choi, S.; Anisur, R. M.; Kim, J.; Lee, I. S. *Angew. Chem. Int. Chem.* **2011**, *50*, 745.

(6) Shao, M. H.; Sasaki, K.; Adzic, R. R. *J. Am. Chem. Soc.* **2006**, *128*, 3526.

(7) Stamenkovic, V. R.; Fowler, B.; Mun, B. S.; Wang, G. F.; Ross, P. N.; Lucas, C. A.; Markovic, N. M. *Science* **2007**, *315*, 493.

(8) Zhang, J.; Sasaki, K.; Sutter, E.; Adzic, R. R. *Science* **2007**, *315*, 220.

(9) Su, F. B.; Tian, Z. Q.; Poh, C. K.; Wang, Z.; Lim, S. H.; Liu, Z. L.; Lin, J. Y. *Chem. Mater.* **2010**, *22*, 832.

(10) Joo, S. H.; Choi, S. J.; Oh, I.; Kwak, J.; Liu, Z.; Terasaki, O.; Ryoo, R. *Nature* **2001**, *412*, 169.

(11) Gupta, G.; Slanac, D. A.; Kumar, P.; Wiggins-Camacho, J. D.; Kim, J.; Ryoo, R.; Stevenson, K. J.; Johnston, K. P. *J. Phys. Chem. C* **2010**, *114*, 10796.

(12) Wen, Z. H.; Liu, J.; Li, J. H. *Adv. Mater.* **2008**, *20*, 743.

(13) Gong, K. P.; Du, F.; Xia, Z. H.; Durstock, M.; Dai, L. M. *Science* **2009**, *323*, 760.

(14) Liu, R. L.; Wu, D. Q.; Feng, X. L.; Mullen, K. *Angew. Chem. Int. Chem.* **2010**, *49*, 2565.

(15) McCreery, R. L. *Chem. Rev.* **2008**, *108*, 2646.

(16) Wu, Z. X.; Hao, N.; Xiao, G. K.; Liu, L. Y.; Webley, P.; Zhao, D. Y. *Phys. Chem. Chem. Phys.* **2011**, *13*, 2495.

(17) Stein, A.; Wang, Z. Y.; Fierke, M. A. *Adv. Mater.* **2009**, *21*, 265.

(18) Wu, Z. X.; Yang, Y. X.; Gu, D.; Li, Q.; Feng, D.; Chen, Z. X.; Tu, B.; Webley, P. A.; Zhao, D. Y. *Small* **2009**, *5*, 2738.

(19) Wu, Z. X.; Zhao, D. Y. *Chem. Commun.* **2011**, *47*, 3332.

(20) Wu, Z. X.; Webley, P. A.; Zhao, D. Y. *Langmuir* **2010**, *26*, 10277.

(21) Joo, S. H.; Kwon, K.; You, D. J.; Pak, C.; Chang, H.; Kim, J. M. *Electrochim. Acta* **2009**, *54*, 5746.

(22) Liu, S. H.; Yu, W. Y.; Chen, C. H.; Lo, A. Y.; Hwang, B. J.; Chien, S. H.; Liu, S. B. *Chem. Mater.* **2008**, *20*, 1622.

(23) Zhou, Z. H.; Wang, S. L.; Zhou, W. J.; Wang, G. X.; Jiang, L. H.; Li, W. Z.; Song, S. Q.; Liu, J. G.; Sun, G. Q.; Xin, Q. *Chem. Commun.* **2003**, 394.

(24) Fang, B. Z.; Kim, J. H.; Kim, M.; Yu, J. S. *Chem. Mater.* **2009**, *21*, 789.

(25) Ding, J.; Chan, K. Y.; Ren, J. W.; Xiao, F. S. *Electrochim. Acta* **2005**, *50*, 3131.

(26) Calvillo, L.; Lazaro, M. J.; Garcia-Bordeje, E.; Moliner, R.; Cabot, P. L.; Esparbe, I.; Pastor, E.; Quintana, J. J. *J. Power Sources* **2007**, *169*, 59.

(27) Kim, H. T.; You, D. J.; Yoon, H. K.; Joo, S. H.; Pak, C.; Chang, H.; Song, I. S. *J. Power Sources* **2008**, *180*, 724.

(28) Steele, B. C. H.; Heinzel, A. *Nature* **2001**, *414*, 345.

(29) Nallathambi, V.; Lee, J. W.; Kumaraguru, S. P.; Wu, G.; Popov, B. N. *J. Power Sources* **2008**, *183*, 34.

(30) Vinu, A. *Top. Catal.* **2010**, *53*, 291.

(31) Shao, Y. Y.; Liu, J.; Wang, Y.; Lin, Y. H. *J. Mater. Chem.* **2009**, *19*, 46.

(32) Gasteiger, H. A.; Kocha, S. S.; Sompalli, B.; Wagner, F. T. *Appl. Catal. B-Environ.* **2005**, *56*, 9.

(33) Joo, S. H.; Pak, C.; You, D. J.; Lee, S. A.; Lee, H. I.; Kim, J. M.; Chang, H.; Seung, D. *Electrochim. Acta* **2006**, *52*, 1618.

(34) (a) Shao, Y. Y.; Zhang, S.; Wang, C. M.; Nie, Z. M.; Liu, J.; Wang, Y.; Lin, Y. H. *J. Power Sources* **2010**, *195*, 4600. (b) Shao, Y. Y.; Zhang, S.; Kou, R.; Wang, X. Q.; Wang, C. M.; Dai, S.; Viswanathan, V.; Liu, J.; Wang, Y.; Lin, Y. H. *J. Power Sources* **2010**, *195*, 1805.

(35) Schaefer, Z. L.; Gross, M. L.; Hickner, M. A.; Schaak, R. E. *Angew. Chem. Int. Chem.* **2010**, *49*, 7045.

(36) Yano, H.; Akiyama, T.; Bele, P.; Uchida, H.; Watanabe, M. *Phys. Chem. Chem. Phys.* **2010**, *12*, 3806.

(37) Gupta, G.; Slanac, D. A.; Kumar, P.; Wiggins-Camacho, J. D.; Wang, X. Q.; Swinnea, S.; More, K. L.; Dai, S.; Stevenson, K. J.; Johnston, K. P. *Chem. Mater.* **2009**, *21*, 4515.

(38) Matsumoto, T.; Komatsu, T.; Nakano, H.; Arai, K.; Nagashima, Y.; Yoo, E.; Yamazaki, T.; Kijima, M.; Shimizu, H.; Takasawa, Y.; Nakamura, J. *Catal. Today* **2004**, *90*, 277.

(39) Wang, S. Y.; Jiang, S. P.; White, T. J.; Guo, J.; Wang, X. *Adv. Funct. Mater.* **2010**, *20*, 1368.

(40) Ignaszak, A.; Ye, S. Y.; Gyenge, E. *J. Phys. Chem. C* **2009**, *113*, 298.

(41) Borup, R.; et al. *Chem. Rev.* **2007**, *107*, 3904.

(42) De Rogatis, L.; Cargnello, M.; Gombac, V.; Lorenzut, B.; Montini, T.; Fornasiero, P. *ChemSusChem* **2010**, *3*, 24.

(43) Wu, Z. X.; Yang, Y. X.; Gu, D.; Zhai, Y. P.; Feng, D.; Li, Q.; Tu, B.; Webley, P. A.; Zhao, D. Y. *Top. Catal.* **2009**, *52*, 12.

(44) Zhao, D. Y.; Feng, J. L.; Huo, Q. S.; Melosh, N.; Fredrickson, G. H.; Chmelka, B. F.; Stucky, G. D. *Science* **1998**, *279*, 548.

(45) Yang, Y. X.; Bourgeois, L.; Zhao, C. X.; Zhao, D. Y.; Chaffee, A.; Webley, P. A. *Microporous Mesoporous Mater.* **2009**, *119*, 39.

(46) (a) Liu, S. H.; Lu, R. F.; Huang, S. J.; Lo, A. Y.; Chien, S. H.; Liu, S. B. *Chem. Commun.* **2006**, 3435. (b) Liu, S. H.; Chen, S. C.; Sie, W. H. *Int. J. Hydrogen Energy* **2011**, *36*, 15060.

(47) Lu, A. H.; Nitz, J. J.; Comotti, M.; Weidenthaler, C.; Schlichte, K.; Lehmann, C. W.; Terasaki, O.; Schuth, F. *J. Am. Chem. Soc.* **2010**, *132*, 14152.

(48) Yu, X.; Ye, S. *J. Power Sources* **2007**, *172*, 133.

(49) Wang, R. H.; Tian, C. G.; Wang, L.; Wang, B. L.; Zhang, H. B.; Fu, H. G. *Chem. Commun.* **2009**, 3104.

(50) Coloma, F.; Sepulvedaescribano, A.; Rodriguezreinoso, F. *J. Catal.* **1995**, *154*, 299.

(51) Choi, W. C.; Woo, S. I.; Jeon, M. K.; Sohn, J. M.; Kim, M. R.; Jeon, H. *J. Adv. Mater.* **2005**, *17*, 446.

(52) Yahikozawa, K.; Fujii, Y.; Matsuda, Y.; Nishimura, K.; Takasu, Y. *Electrochim. Acta* **1991**, *36*, 973.

(53) Kinoshita, K. *J. Electrochem. Soc.* **1990**, *137*, 845.